

GRB 190114C: from prompt to afterglow?

M. E. Ravasio^{1,2}, G. Oganessian^{3,4}, O. S. Salafia^{1,2}, G. Ghirlanda^{1,2}, G. Ghisellini¹, M. Branchesi^{3,4}, S. Campana¹, S. Covino¹, R. Salvaterra⁵

¹ INAF – Osservatorio Astronomico di Brera, via E. Bianchi 46, I-23807 Merate, Italy.

² Dipartimento di Fisica G. Occhialini, Univ. di Milano Bicocca, Piazza della Scienza 3, I-20126 Milano, Italy.

³ Gran Sasso Science Institute, Viale F. Crispi 7, I-67100, L'Aquila, Italy

⁴ INFN - Laboratori Nazionali del Gran Sasso, I-67100, L'Aquila, Italy

⁵ INAF - Istituto di Astrofisica Spaziale e Fisica Cosmica, via E. Bassini 15, I-20133 Milano, Italy

ABSTRACT

GRB 190114C is the first gamma-ray burst detected at Very High Energies (VHE, i.e. > 300 GeV) by the MAGIC Cherenkov telescope. The analysis of the emission detected by the *Fermi* satellite at lower energies, in the 10 keV – 100 GeV energy range, up to ~ 50 seconds (i.e. before the MAGIC detection) can hold precious information. We analyse the spectral evolution of the emission of GRB 190114C as detected by the *Fermi* Gamma-Ray Burst Monitor (GBM) in the 10 keV – 40 MeV energy range up to ~ 60 sec. The first 4 seconds of the burst feature a typical prompt emission spectrum, which can be fitted by a smoothly broken power-law function with typical parameters. Starting on ~ 4 seconds post-trigger, we find an additional non-thermal component, which can be fit by a power-law, which rises and decays quickly. The 10 keV – 40 MeV flux of the power-law component peaks at ~ 6 seconds reaching the value of $1.7 \times 10^{-5} \text{ erg cm}^{-2} \text{ s}^{-1}$. The time when it peaks coincides with the peak of the emission detected by the Large Area Telescope (LAT) on board *Fermi*. The power-law spectral slope that we find in the GBM data is remarkably similar to that of the LAT spectrum and the GBM+LAT spectral energy distribution seems to be consistent with a single component. This suggests that the LAT emission and the power law component that we find in the GBM data belong to the same emission component, which we interpret as due to the afterglow of the burst. The onset time allows us to estimate the initial jet bulk Lorentz factor Γ_0 to be around 500, depending on the assumed circum-burst density.

Key words. gamma-ray burst: general – radiation mechanisms: non-thermal – gamma-ray burst: individual

1. Introduction

Soon after its launch, the *Fermi* satellite has been detecting¹ on average ~ 14 Gamma-Ray Bursts (GRBs) per year with its Large Area Telescope (LAT) in the High Energy (HE) range between few MeV up to 100 GeV (Ackermann et al. 2013). *Fermi*/LAT GRBs confirm detections by the Astro Rivelatore Gamma ad Immagini Leggero (Agile)/GRID – Giuliani et al. 2008, 2010; Del Monte et al. 2011) and the earlier results of the *Compton Gamma Ray Observatory*/EGRET (Sommer et al. 1994; Hurley et al. 1994; González et al. 2003). Until only recently, observations of GRBs emission at Very High Energies (VHE) by Imaging Atmospheric Cherenkov Telescopes (IACT) resulted only in upper limits (Aliu et al. 2014, Carosi et al. 2015; Hoischen et al. 2017). GRB 190114C is the first burst detected at > 300 GeV by the Major Atmospheric Gamma Imaging Cherenkov Telescopes (MAGIC) (Mirzoyan et al. 2019).

GRB emission in the 100 MeV – 100 GeV energy range, as detected by LAT, typically starts with a small delay with respect to the trigger time of the keV–MeV component (Omodei 2009; Ghisellini et al. 2010; Ghirlanda et al. 2010), and extends after the prompt emission. This behaviour has been also observed in short GRBs (Ghirlanda et al. 2010; Ackermann et al. 2010a). While the early HE emission (simultaneous to the keV–MeV component) shows some vari-

ability, its long-lasting tail exhibits a smooth decay in time. A possible transition from an early steep decay ($\propto t^{-1.5}$) to a shallower regime ($\propto t^{-1}$) has been reported (Ghisellini et al. 2010; Ackermann et al. 2013) and a faster temporal decay in brighter bursts has been claimed (Panaitescu 2017).

During the prompt emission phase (as detected by e.g. the Gamma Ray Burst Monitor – GBM – onboard the *Fermi* satellite) the LAT spectrum can either be the extension, above 100 MeV, of the typical sub-MeV GRB spectrum (which is usually fitted with the Band function – Band et al. 1993) or else it requires an additional spectral component in the form of a power-law (PL) as in GRB 080916C, 110713A (Ackermann et al. 2013), 090926A (Yasine et al. 2017) and 130427A (Ackermann et al. 2014). In few bursts, this additional PL component has been found extending to the X-ray range (< 20 keV – e.g. 090510 – Ackermann et al. 2010a, 090902B – Abdo et al. 2009). The LAT spectrum, when the prompt emission is ceased, is often fitted by a power-law with photon index $\Gamma_{\text{PL}} \sim -2$.

The interpretation of the HE emission of GRBs is still under debate (see Nava et al. 2017 for a review). It has been proposed that the LAT emission extending after the end of the prompt is the afterglow produced in the external shock driven by the jet into the circum-burst medium (Kumar & Barniol Duran 2009; Ghisellini et al. 2010; Kumar & Barniol Duran 2010), the emission mechanism possibly being synchrotron. The correlation of the LAT luminosity

¹http://fermi.gsfc.nasa.gov/ssc/observations/types/grbs/lat_grbs/table.php.

with the prompt emission energy (Nava et al. 2014) and the direct modelling of the broad band spectral energy distribution (initially in few bursts Kumar & Barniol Duran 2009, 2010 and then on a larger sample Beniamini et al. 2015) support the synchrotron origin.

A possible problem with the synchrotron interpretation is the detection of very high energy photons (tens of GeV), greater than the theoretical limit of synchrotron emission from shock accelerated electrons. This limit is ~ 70 MeV in the comoving frame (Guilbert et al. 1983, see also de Jager et al. 1996; Lyutikov 2010 who find a lower value ~ 30 MeV) but downstream magnetic field stratification (Kumar et al. 2012) or acceleration in magnetic reconnection layers (Uzdensky et al. 2011; Cerutti et al. 2013) can alleviate this apparent tension.

The deceleration of the jet by the interstellar medium should produce a peak in the afterglow light curve at a time t_p , corresponding to the transition from the coasting to the deceleration phase (Sari & Piran 1999). t_p depends on the blast wave kinetic energy E_k , on the density of the circum-burst medium (and its radial profile) and on the initial bulk Lorentz factor Γ_0 (representing the maximum velocity that the jet attained, i.e. that of the coasting phase). Therefore, by deducing E_k from the prompt emission and making an assumption on the circum-burst medium density, it is possible to estimate Γ_0 (Molinari et al. 2007; Ghirlanda et al. 2012, 2018) for large samples of GRBs.

If the GeV component is afterglow due to the external shock, the time t_p provides an estimate of Γ_0 (see also Nava et al. 2017), as shown for the first time in the case of the LAT detected GRB 090510 (Ghirlanda et al. 2010). The shorter t_p , the larger Γ_0 : LAT bursts have the shortest times t_p (Ghirlanda et al. 2018) and therefore provide the largest values of Γ_0 up to ~ 1200 (GRB 090510 – Ghirlanda et al. 2018). As discussed in Ghisellini et al. (2010), this might indicate that a large Γ_0 helps to accelerate very high energy electrons, which emit at large photon energies. Furthermore, even a small fraction of photons of the prompt phase can be scattered by the circum-burst medium and act as targets for the $\gamma\text{-}\gamma \rightarrow e^\pm$ process: this enhances the lepton abundance of the medium, thus making shock acceleration of the leptons more efficient (Beloborodov 2005; Ghisellini et al. 2010).

While the LAT emission, detected in some cases up to hours after the end of the prompt, seems to be of external origin, a possible challenge is the interpretation of the early LAT emission, detected during the prompt phase. It has been argued (Zhang et al. 2011; He et al. 2011) that the very early LAT emission has an internal origin (Bošnjak et al. 2009) as it can be due to Inverse Compton scattered synchrotron photons of the prompt (SSC). The delay of the GeV emission, as measured by LAT, could be accounted by Inverse Compton emission occurring in the Klein–Nishina regime at early times (Daigne 2012; Bošnjak et al. 2009). While recent findings seem to support a synchrotron origin of keV–MeV photons (Oganesyan et al. 2017, 2018; Ravasio et al. 2018), the presence of a soft excess (< 50 keV), clearly seen so far in GRB 090902B (Abdo et al. 2009) GRB 090510 (Ackermann et al. 2010b) and GRB 090926A (Yassine et al. 2017), represents a challenge for the SSC interpretation (but see Toma et al. 2011) and would be more easily interpreted as the low energy extension of the GeV afterglow component.

This paper is based on the study the emission of GRB 190114C (§2) as detected by the GBM in the 10 keV – 40 MeV energy range, up to 61 seconds after the trigger. We also consider data from the Burst Alert Telescope (BAT) and the X-Ray Telescope (XRT) onboard the *Neil Gehrels Swift Observatory* in three time intervals. While the properties of GRB 190114C are similar to other bursts detected by LAT, the presence of emission possibly extending up to the TeV energy range, as detected by MAGIC (Mirzoyan et al. 2019), makes this event unique so far. Data extraction and analysis are presented in §3 and in §4, where we show the appearance and temporal evolution of a non-thermal power-law spectral component starting from 4 s after the trigger. In §5 we discuss our results and their implications.

2. GRB 190114C

On January 14 2019 at 20:57:03 UT both the *Fermi*/GBM and the *Swift*/BAT were triggered by GRB 190114C (Hamburg et al. 2019; Gropp et al. 2019). The burst was detected in hard X-rays also by the SPI-ACS instrument onboard *INTEGRAL*, with evidence for long-lasting emission (Minaev & Pozanenko 2019), by the Mini-CALorimeter (MCAL) instrument onboard the *AGILE* satellite (Ursi et al. 2019), by the Hard X-ray Modulation Telescope (HXMT) instrument onboard the *Insight* satellite (Xiao et al. 2019) and by Konus-Wind (Frederiks et al. 2019).

Remarkably, this burst was the first to be detected at very high energies by a Cherenkov telescope: MAGIC was able to point the source 50 seconds after the *Swift* trigger, revealing the burst with a significance $> 20\sigma$ at energies > 300 GeV (Mirzoyan et al. 2019). The burst was also detected by LAT, remaining in its field of view until 150 s after the GBM trigger (Kocevski et al. 2019).

The redshift was first measured by the Nordic Optical Telescope (NOT) (Selsing et al. 2019) and soon confirmed by the Gran Telescopio Canarias (GTC, Castro-Tirado et al. 2019), with $z = 0.4245 \pm 0.0005$.

The fluence (integrated in the 10–1000 keV energy range) measured by the GBM is $3.99 \times 10^{-4} \pm 8 \times 10^{-7}$ erg cm^{-2} and the peak photon flux (with 1 s binning on the same energy range) is 246.86 ± 0.86 $\text{cm}^{-2} \text{s}^{-1}$ (Hamburg et al. 2019). As reported in Hamburg et al. 2019, the corresponding isotropic equivalent energy and luminosity are $E_{\text{iso}} \sim 3 \times 10^{53}$ erg and $L_{\text{iso}} \sim 1 \times 10^{53}$ erg s^{-1} , respectively. These values make this burst consistent with the $E_{\text{peak}}\text{--}E_{\text{iso}}$ (Amati et al. 2002) and $E_{\text{peak}}\text{--}L_{\text{iso}}$ (Yonetoku et al. 2004) correlations (Frederiks et al. 2019).

The prompt emission of GRB 190114C is characterized by a first (multi-peaked) pulse lasting ~ 5.5 seconds, followed by a second weaker and softer pulse from 15 to 22 seconds after trigger (as shown in the top panel of Fig. 1), and then a weaker and long tail lasting up to hundreds of seconds (Hamburg et al. 2019; Minaev & Pozanenko 2019).

3. Data analysis

3.1. *Fermi*/GBM

3.1.1. Data extraction

The GBM is composed of 12 sodium iodide (NaI, 8 keV–1 MeV) and 2 bismuth germanate (BGO, 200 keV–40 MeV) scintillation detectors (Meegan et al. 2009). We analyzed

the data of the three brightest NaI detectors with a viewing angle less than 60° (n3, n4, n7) and both the BGO detectors (b0 and b1). In particular, we selected the energy channels in the range 8–900 keV for NaI detectors, excluding the channels in the range 25–40 keV due to the presence of the Iodine K-edge at 33.17 keV², and 0.3–40 MeV for BGO detectors. Spectral data files and the corresponding response matrix files (.rsp2) are obtained from the online archive³ and the spectral analysis has been performed with the public software RMFIT- (v. 4.3.2). To model the background, we select background spectra in time intervals well before and after the burst (approximately -130 : -10 s and 210 : 370 s from the trigger time) and model them with a polynomial function up to the third-order. We use TTE (Time Tagged Event) data, rebinning them with a time resolution of 0.3 s during the first emission episode of the burst. After the first emission episode, we rebinned the data in progressively larger time bins up to the second minor peak of the light curve (from ~ 15 s to ~ 23 s), that has been analyzed as a single bin. Finally, we analyzed the 23–61 s time interval as two consecutive time bins (23–47 s and 47–61 s).

3.2. Swift: BAT and XRT data

We consider also BAT data extracted for three time bins, namely 6–6.3 s, 47–61 s and 87–232 s, both as a check of the consistency with the parameters of the fit obtained in the same time intervals from GBM data, and as a way to extend our analysis to later times. We downloaded BAT event files from the *Swift* data archive⁴. To extract BAT spectra, we used the latest version of the HEASOFT package (v6.25). We generate BAT spectral files by the `batbinevt` task, applying the correction for systematic errors with the `batupdatephakw` and `batphasyserr` tasks. We generate response files with the `batdrmgrn` tool. We adopt the latest calibration files (CALDB release 2017–10–16).

In addition, we retrieved XRT event files from the *Swift*/XRT archive⁵. The source and background files have been extracted by the `xselect` tool. We removed the central region of XRT image to avoid the pile-up effects, following the procedure described in Romano et al. (2006). We generated an ancillary response file by the `xrtmkarf` task. We excluded all the channels below 1.5 keV since an apparent low-energy excess has been reported in Beardmore (2019). We then re-binned the energy channels using the `grppha` tool requiring at least 40 counts per bin.

We used the multiplicative XSPEC models `tbabs` and `ztbabs` to account for Galactic and intrinsic absorption of the X-ray spectrum by neutral hydrogen (Wilms et al. 2000). The value of Galactic neutral hydrogen column density in the direction of GRB 190114C is found from Kalberla et al. (2005). The intrinsic column density $7.7 \times 10^{22} \text{cm}^{-2}$ is estimated by fitting the late-time X-ray spectrum ($5.6 \times 10^4 - 5.7 \times 10^5$ s).

3.2.1. Fitting models

A preliminary analysis of the GBM spectrum was reported in Hamburg et al. (2019): the time-integrated spectrum from 0 to 38.59 s (that includes all the two pulses of the burst but also the inter-pulse interval) is fitted with a Band function, finding $E_{\text{peak}} = 998.6 \pm 11.9$ keV, $\alpha = -1.058 \pm 0.003$, and $\beta = -3.18 \pm 0.07$. In addition, they also report a strong statistical preference for the existence of an extra power-law component.

In our time-resolved analysis, we fit the spectra with a smoothly broken power-law (SBPL, see Ravasio et al. 2018 for a description of the functional form). The SBPL is one of the empirical functions generally used to model GRB spectra (Kaneko et al. 2006; Gruber et al. 2014). The SBPL is made of two power-laws, with spectral indices α and β , smoothly connected at the break energy (usually corresponding to the νF_ν peak of the spectrum, E_{peak}). As in Ravasio et al. 2018, the curvature parameter is kept fixed at $n = 2$.

Given the possible presence of an extra power-law component reported in Hamburg et al. (2019), we also added an extra power-law component in the fitting procedure, with two free parameters, namely the normalization N and the spectral index Γ_{PL} .

4. Results

Fig. 1 shows the results of the time resolved spectral analysis of GBM data. We find that all spectra belonging to the first emission episode (from 0 s to 4.8 s) are reasonably well fitted by a SBPL model without the need of an additional power-law component. The low and high energy spectral indices of the SBPL model are shown in panel (C) of Fig. 1 (red and black symbols respectively). Their values are consistent with the typical distributions obtained by the analysis of large samples of GBM bursts (Goldstein et al. 2012; Gruber et al. 2014; Nava et al. 2011; Kaneko et al. 2006). The peak energy (panel D in Fig. 1) evolves tracking the flux of the light curve, with an average value of $E_{\text{peak}} = 510 \pm 170$ keV.

The presence of the additional power-law component starts in the 4.8–5.4 s and 5.4–6.0 s time bins, where the superposition of a SBPL and a PL component is preferred over the SBPL component alone (an F-test yields a 6 and 7.5 σ preference for the SBPL+PL model in the first and second bin, respectively).

The power-law component reaches its peak in the time bin 6–6.3 s, with a flux of $1.7 \pm 0.2 \times 10^{-5} \text{erg cm}^{-2} \text{s}^{-1}$, integrated in the energy range 10 keV–40 MeV. From 6.3 s onward, the spectrum is well fitted (p-value > 0.3 in all bins) by a single power-law PL component, with no increase in the goodness of fit when adding the SBPL component. Moreover, when we try to fit with the SBPL function, the peak energy E_{peak} is completely unconstrained, and the values found for the two spectral indices α and β are consistent with each other within the errors. The single power-law spectral slope is shown by the blue symbols in panel (C) of Fig. 1. Its 10 keV – 40 MeV flux is shown by the blue symbols in panel (B).

The average spectral slope of the PL component in the time interval 4.8–15.3 s is $\Gamma_{\text{PL}} = -1.81 \pm 0.08$, similar to the spectral slope found in the LAT data (at > 100 MeV, Kocovski et al. 2019) in the same time interval (Wang et al.

²https://fermi.gsfc.nasa.gov/ssc/data/analysis/GBM_caveats.html

³<https://heasarc.gsfc.nasa.gov/W3Browse/fermi/fermigbrst.html>

⁴<http://heasarc.gsfc.nasa.gov/cgi-bin/W3Browse/swift.pl>

⁵<http://www.swift.ac.uk/archive/>

2019). After ~ 10 seconds the slope of the power-law becomes constant and settles to the -2 value, again similar to the LAT index. The second emission episode is fitted by a SBPL, with $\alpha = -1.51 \pm 0.06$, $\beta = -2.33 \pm 0.06$ and $E_{\text{peak}} = 63 \pm 3$ keV. The parameters of the additional power-law are not constrained and the fit does not improve with its inclusion. After 22.8 s, the spectrum is again well fitted by a power-law only, with index $\Gamma_{\text{PL}} \sim -2$. The flux of the PL component (panel B of Fig. 1) decays steeply from the peak up to 15 seconds (a reference green line $\propto t^{-2.8}$ is shown). From 15–50 seconds the flux temporal decay is consistent with $t^{-1.0}$.

We also added BAT data for the time intervals 6.0–6.3 s and 11–14 s. In both time bins, BAT+GBM data have been fitted together with a single PL, obtaining best fit parameters which are consistent with the analysis of GBM data only. We also verified that BAT data alone for the first time bin result in power-law parameters which are fully consistent with those derived from the fit of the GBM spectrum alone. Fig. 2 shows the spectral energy distribution of the three time intervals (as labelled). Spectral data used in the fits are BAT+GBM for interval 6–6.3 s and 11–14 s, XRT+BAT+GBM spectra are shown for the last time bin (66–92 s). Wang et al. (2019) performed the analysis of the LAT spectrum of GRB 190114C, fitting the high energy data with a power-law model. Fig. 2 also shows with butterfly symbols the LAT flux and spectral index (including the corresponding uncertainties) for the same time intervals, to be compared with our results.

Both GBM and BAT data appear to connect to the LAT emission as analyzed by Wang et al. (2019). Regarding the two time intervals, 6–6.3 s and 11–14 s, the photon indices of the LAT spectrum are $\Gamma_{\text{PL}} = -2.06 \pm 0.30$ and $\Gamma_{\text{PL}} = -2.10 \pm 0.31$ respectively, which are consistent with the values we obtained from our analysis. The LAT emission is slightly above the GBM extrapolation (by less than 60%, namely less than 2σ). Moreover, we analyzed XRT+BAT+GBM data from 66 s to 92 s, to check again for consistency with the LAT flux given in Wang et al. (2019) and also to track the power-law evolution at later times. As shown in Fig. 2, the LAT flux is still consistent with extrapolation of the joint XRT+BAT+GBM data fit. From our analysis, the fit of XRT+BAT+GBM data from 66 s to 92 s with a PL function results in a spectral slope $\Gamma_{\text{PL}} = -2.01 \pm 0.05$, which is only marginally consistent with the values obtained by Wang et al. (2019) for the LAT data ($\Gamma_{\text{PL}} = -1.67 \pm 0.27$). Note though that the spectral slopes reported in Wang et al. (2019) have large uncertainties and show a rapid variability. In summary, Fig. 2 shows that the keV–MeV and GeV emissions have similar time decay and similar slopes, suggesting that they belong to the same component. However, due to the uncertainties on the LAT spectral parameters reported in Wang et al. (2019), it cannot be excluded the possibility that the GeV and keV–MeV data belong to two different components.

4.1. Estimate of Γ_0

There are several slightly different formulae to derive the bulk Lorentz factor Γ_0 of the coasting phase from the observational data. The required parameters are: i) the time of the peak of the light curve t_p ; ii) the isotropic equivalent kinetic energy of the jet E_K after the emission of the prompt

radiation; iii) the circum-burst density n , responsible for the deceleration of the jet, and iv) its radial profile.

Usually, one assumes that the observed, isotropic equivalent energy radiated in the prompt phase E_{iso} is a fraction η of the kinetic energy, implying $E_K = E_{\text{iso}}/\eta$, typically with $\eta = 0.1$ or 0.2 . The density is assumed to have a radial profile $n \propto R^{-s}$ (R is the distance from the central engine originating the GRB). We will consider the case of a uniform density ($s = 0$), or a steady stellar wind density profile ($s = 2$). In the latter case the density depends on the mass rate \dot{M}_w of the wind and its velocity v_w (Chevalier & Li 2000), namely $n(R) = \dot{M}_w / (4\pi v_w R^2 m_p)$.

The different formulae used to calculate Γ_0 have been thoroughly discussed in Ghirlanda et al. (2018). As in that paper, we use the formula derived in Nava et al. (2013):

$$\Gamma_0 = \left[\frac{(17 - 4s)(9 - 2s)3^{2-s}}{2^{10-2s}\pi(4-s)} \left(\frac{E_K}{n_0 m_p c^5} \right) \right]^{\frac{1}{8-2s}} t_{p,z}^{-\frac{3-s}{8-2s}} \quad (1)$$

that, for the two different cases of homogeneous medium ($s=0$) and wind density profile ($s=2$), becomes:

$$\Gamma_0 \propto \left(\frac{E_{\text{iso}}}{\eta n_0 m_p c^5} \right)^{\frac{1}{8}} t_{p,z}^{-\frac{3}{8}} \quad (s = 0) \quad (2)$$

$$\Gamma_0 \propto \left(\frac{E_{\text{iso}}}{\eta n_0 m_p c^3} \right)^{\frac{1}{4}} t_{p,z}^{-\frac{1}{4}} \quad (s = 2) \quad (3)$$

Here t_p is measured in the source cosmological rest frame, i.e. $t_{p,z} = t_p/(1+z)$, m_p is the mass of the proton, and n_0 is the normalization of the circum-burst density profile, i.e. $n(R) = n_0 R^{-s}$.

Assuming $E_{\text{iso}} = 2.6 \times 10^{53}$ erg calculated from 0 to 6 s, $\eta = 0.2$, $t_p = 6$ s, through Eq. 1 we estimate: $\Gamma_0 \sim 700 \pm 26$ (resp. 520 ± 20) in the case of a homogeneous medium with density $n = 1 \text{ cm}^{-3}$ (resp. $n = 10 \text{ cm}^{-3}$). For a wind medium with $\dot{M}_w = 10^{-5} M_\odot/\text{yr}$ and $v_w = 10^3 \text{ km/s}$ (resp. $v_w = 10^2 \text{ km/s}$), following the relation $n_0 = \dot{M}_w / 4\pi v_w m_p$, the initial bulk Lorentz factor is $\Gamma_0 \sim 230 \pm 6$ (resp. 130 ± 3). The errors are only statistical and are calculated using the uncertainties on the observables E_{iso} and t_p ; the errors do not include the unknown uncertainties on the η and n_0 parameters.

Table 2 in Ghirlanda et al. (2018) gives the coefficients needed to calculate Γ_0 for all the other proposed formulae, both for the homogeneous and for the wind case. The resulting Γ_0 values differ at most by a factor of 2. The computed values are similar to those found for other GRBs detected by LAT which show a peak in the light curve in the LAT energy band (Ghirlanda et al. 2018).

5. Discussion

Our results point to the presence, in the GBM data, of a power-law component appearing at ~ 4 s after trigger, peaking at 6 s, and then declining. This temporal behaviour matches that of the flux above 100 MeV, as seen by the LAT. Fig. 2 shows that the emission in the two detectors (GBM and LAT) joins smoothly, with a consistent slope

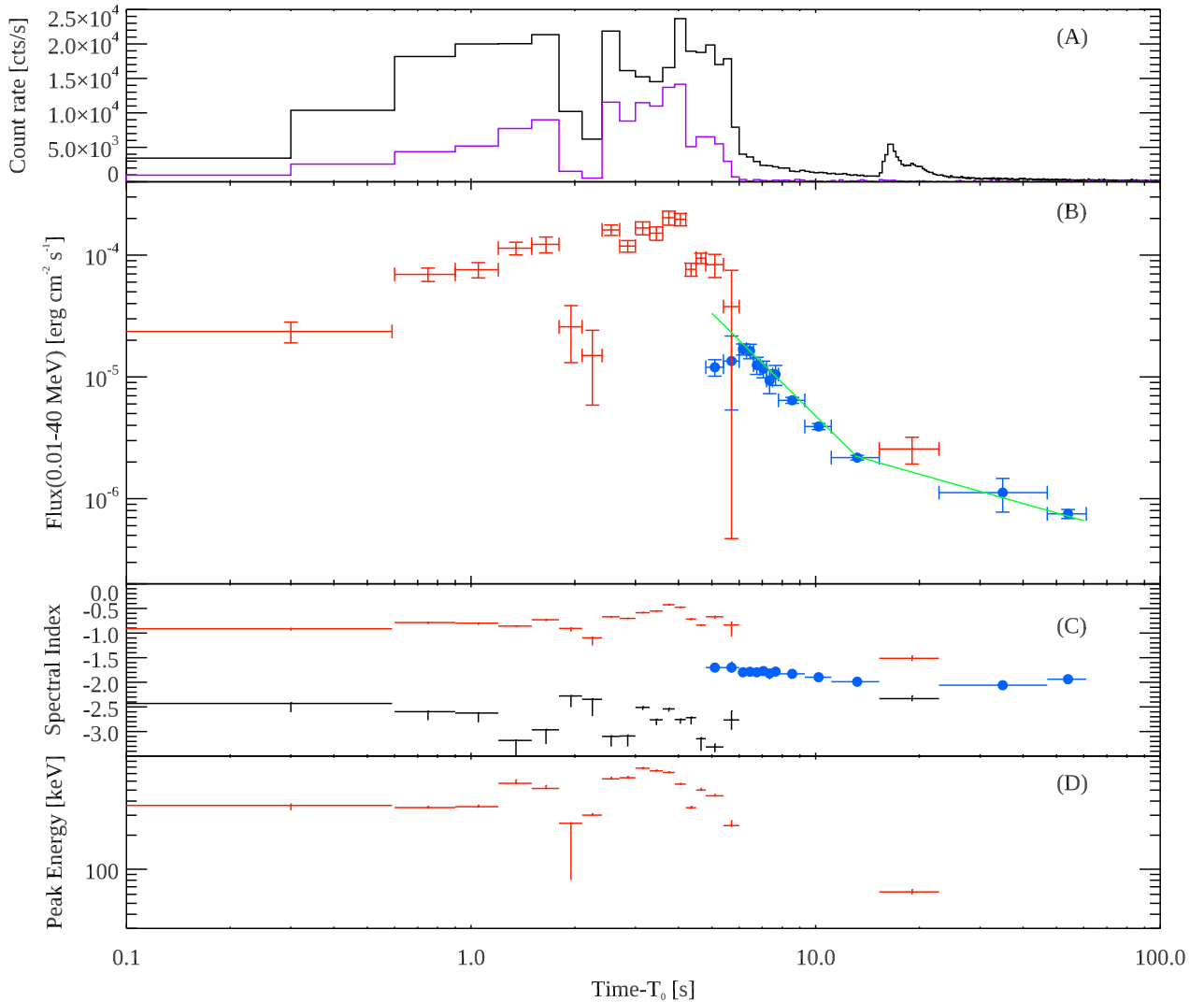


Fig. 1. Spectral evolution of GRB190114C. Two spectral components are shown: Smoothly broken power-law (SBPL - red symbols) and Power law (PL - blue circles). 1σ errors are shown. Panel A: count rate light curve (black solid line for GBM NaI detector #3 and purple solid line for GBM BGO detector #0). Panel B: flux (integrated in the 10 keV – 40 MeV energy range) of the two spectral components. The green line is a power-law with slope -2.8 up to 15 seconds, with slope -1 when the decay of the flux is shallower. Panel C shows the temporal evolution of the spectral photon index of the SBPL (red and black symbols) and of the PL (blue symbols). Panel D shows the evolution of the peak energy (E_{peak}) of the SBPL model.

(within the errors). It is therefore compelling to interpret the two power-laws seen in LAT and GBM as belonging to a single emission component. We propose this non-thermal emission to be produced by the external shock driven by the jet into the circum-burst medium, with its peak marking the jet deceleration time, i.e. onset time of the afterglow.

The reasons leading to this interpretation are: i) they appear after the trigger of the prompt event, and peak when most of the prompt emission energy has already been radiated; ii) they last much longer than the prompt emission; iii) they are characterized by a spectral index ($\Gamma_{PL} \sim -2$) typical of the known afterglows; iv) with the exception of the early, variable phases, their light curve is smoothly decaying with a temporal slope typical of the known afterglows.

We remark that this is not the first time that a power-law shows up in the hard X-rays, in addition to the spectral components usually seen during the prompt emission phase.

In fact, such a component was well visible in GRB 090202B, another burst which was very strong in the LAT band (Rao et al. 2013 and references above). What is new is the observation of the onset of the afterglow in the hard X-ray band, found to be simultaneous, within the uncertainties, to the peak of the LAT light-curve. This is especially important in this burst, because of the MAGIC detection.

Our results imply that emission in the energy range between 10 keV and 30 GeV is produced by a single mechanism. If such mechanism is synchrotron or inverse Compton, this in turn implies that the energy of the underlying electron distribution must extend over more than three orders of magnitude.

We also know that the MAGIC telescope revealed photons above 300 GeV (Mirzoyan et al. 2019), despite the strong absorption due to the extragalactic optical-infrared background (e.g. Franceschini et al. 2008) expected for

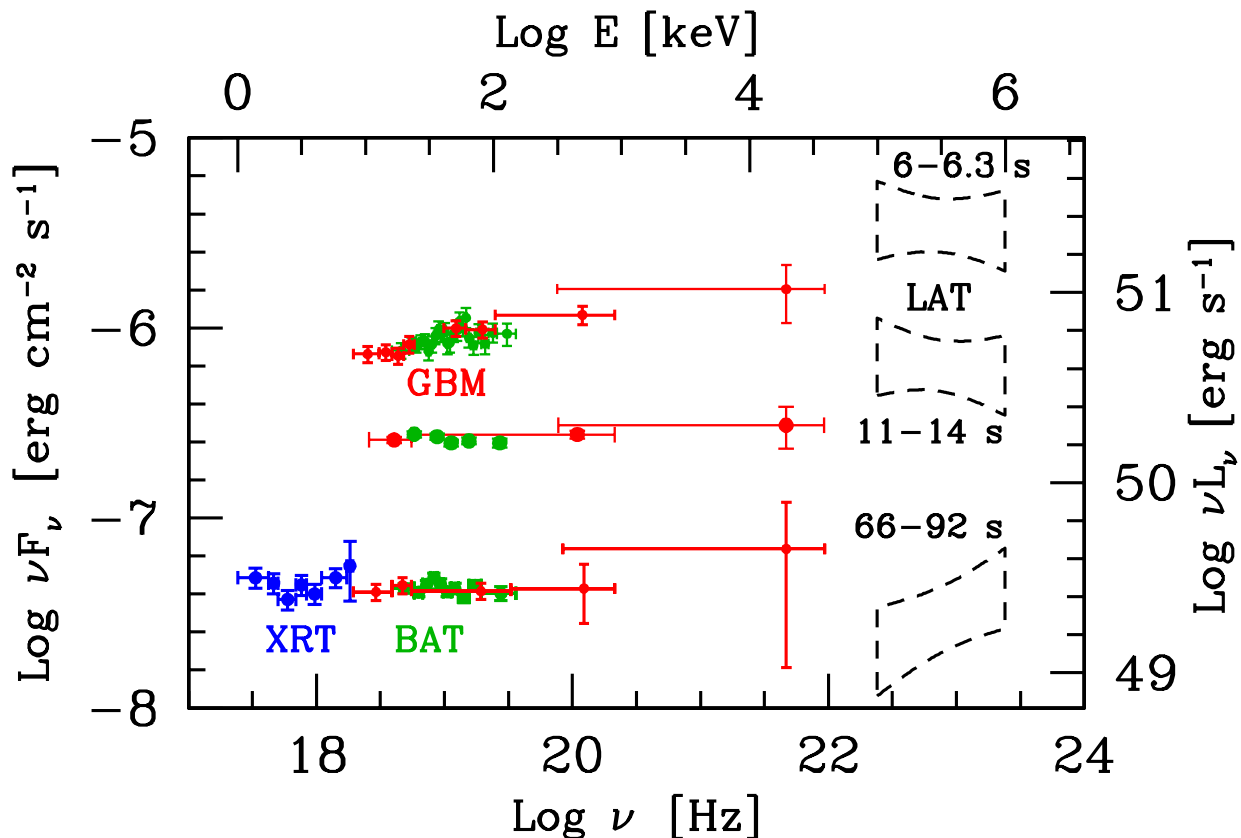


Fig. 2. The X-ray to GeV SED of GRB 190114C at three specific times: at 6-6.3 s, when the power-law component has its peak in the GBM data (see panel (B) of Fig.1, blue symbols), at 11-14 s and at 66-92 s (as labelled). We show the GBM, BAT and XRT data (the latter de-absorbed as described in the text). Errors and upper limits on the data points represent 1σ . The LAT butterflies represent the range of fluxes and indices of the power-law reported in analysis of Wang et al. (2019).

$z = 0.425$. If we believe that the maximum synchrotron energy is $h\nu_{\max} = m_e c^2 / \alpha_F \sim 70$ MeV in the comoving frame, as theoretically predicted in the case of shock acceleration (Guilbert et al. 1983; de Jager et al. 1996), then we are led to interpret the radiation above 300 GeV as due to another process, most likely inverse Compton or synchrotron self-Compton. On the other hand, the observed maximum photon energy detected by LAT, 22.9 GeV 15 s after trigger, does not violate the comoving 70 MeV limit if the bulk Lorentz factor Γ at this time is larger than 450. For this value to be consistent with Γ_0 , i.e. the bulk Lorentz of the jet before it starts to be decelerated by the circum-burst medium, we need (assuming a prompt efficiency $\eta = 0.2$) the circum-burst medium to be not too dense, with a number density $n \lesssim 30 \text{ cm}^{-3}$ in the homogeneous case, or the progenitor stellar wind to be slightly faster and/or less massive than usually assumed, to satisfy $\dot{M}_{w,-5} v_{w,8} \lesssim 0.02$ (where $\dot{M}_{w,-5} = \dot{M}_w / (10^{-5} M_\odot \text{ yr}^{-1})$ and $v_{w,8} = v_w / (10^8 \text{ cm s}^{-1})$).

Alternatively, the entire SED from the keV to the TeV energy range could be inverse Compton emission, possibly by Compton scattering off IR-optical radiation. In this case the MAGIC emission should connect smoothly with the LAT spectrum (i.e., namely, it should not be harder). Therefore the MAGIC flux and spectrum will give crucial

information about the origin of the entire high energy spectrum of Gamma-Ray Bursts.

Acknowledgments

We would like to thank Lara Nava for fruitful discussions. M. E. R. is thankful to the Observatory of Brera for the kind hospitality. This research has made use of data obtained through the High Energy Astrophysics Science Archive Research Center Online Service, provided by the NASA/Goddard Space Flight Center, and specifically this work made use of public *Fermi*-GBM data. We acknowledge INAF-Prin 2017 (1.05.01.88.06) for support and the Italian Ministry for University and Research grant "FIGARO" 1.05.06.13. We also would like to thank for support the implementing agreement ASI-INAF n.2017-14-H.0.

References

- Abdo, A. A., Ackermann, M., Asano, K., et al. 2009, *ApJ*, 707, 580
- Ackermann, M., Ajello, M., Asano, K., et al. 2014, *Science*, 343, 42
- Ackermann, M., Ajello, M., Asano, K., et al. 2013, *ApJS*, 209, 11
- Ackermann, M., Asano, K., Atwood, W. B., et al. 2010a, *ApJ*, 716, 1178
- Ackermann, M., Asano, K., Atwood, W. B., et al. 2010b, *ApJ*, 716, 1178
- Aliu, E., Aune, T., Barnacka, A., et al. 2014, *ApJ*, 795, L3

- Amati, L., Frontera, F., Tavani, M., et al. 2002, *A&A*, 390, 81
- Band, D., Matteson, J., Ford, L., et al. 1993, *ApJ*, 413, 281
- Beardmore, A. P. 2019, GRB Coordinates Network, Circular Service, No. 23736, #1 (2019), 23736
- Beloborodov, A. M. 2005, *ApJ*, 627, 346
- Beniamini, P., Nava, L., Duran, R. B., & Piran, T. 2015, *MNRAS*, 454, 1073
- Bošnjak, Ž., Daigne, F., & Dubus, G. 2009, *A&A*, 498, 677
- Carosi, A., Antonelli, A., Becerra Gonzalez, J., et al. 2015, in *International Cosmic Ray Conference*, Vol. 34, 34th International Cosmic Ray Conference (ICRC2015), ed. A. S. Borisov, V. G. Denisova, Z. M. Guseva, E. A. Kanevskaya, M. G. Kogan, A. E. Morozov, V. S. Puchkov, S. E. Pyatovsky, G. P. Shoziyoev, M. D. Smirnova, A. V. Vargasov, V. I. Galkin, S. I. Nazarov, & R. A. Mukhamedshin, 809
- Castro-Tirado, A. J., Hu, Y., Fernandez-Garcia, E., et al. 2019, GRB Coordinates Network, Circular Service, No. 23708, #1 (2019), 23708
- Cerutti, B., Werner, G. R., Uzdensky, D. A., & Begelman, M. C. 2013, *ApJ*, 770, 147
- Chevalier, R. A. & Li, Z.-Y. 2000, *ApJ*, 536, 195
- Daigne, F. 2012, in *International Journal of Modern Physics Conference Series*, Vol. 8, International Journal of Modern Physics Conference Series, 196–208
- de Jager, O. C., Harding, A. K., Michelson, P. F., et al. 1996, *ApJ*, 457, 253
- Del Monte, E., Barbiellini, G., Donnarumma, I., et al. 2011, *A&A*, 535, A120
- Franceschini, A., Rodighiero, G., & Vaccari, M. 2008, *A&A*, 487, 837
- Frederiks, D., Golenetskii, S., Aptekar, R., et al. 2019, GRB Coordinates Network, Circular Service, No. 23737, #1 (2019), 23737
- Ghirlanda, G., Ghisellini, G., & Nava, L. 2010, *A&A*, 510, L7
- Ghirlanda, G., Nappo, F., Ghisellini, G., et al. 2018, *A&A*, 609, A112
- Ghirlanda, G., Nava, L., Ghisellini, G., et al. 2012, *MNRAS*, 420, 483
- Ghisellini, G., Ghirlanda, G., Nava, L., & Celotti, A. 2010, *MNRAS*, 403, 926
- Giuliani, A., Fuschino, F., Vianello, G., et al. 2010, *ApJ*, 708, L84
- Giuliani, A., Mereghetti, S., Fornari, F., et al. 2008, *A&A*, 491, L25
- Goldstein, A., Burgess, J. M., Preece, R. D., et al. 2012, *ApJS*, 199, 19
- González, M. M., Dingus, B. L., Kaneko, Y., et al. 2003, *Nature*, 424, 749
- Gropp, J., Kennea, J. A., K. N. J., Krimm, H. A., et al. 2019, GRB Coordinates Network, Circular Service, No. 23688, #1 (2019), 23688
- Gruber, D., Goldstein, A., Weller von Ahlefeld, V., et al. 2014, *The Astrophysical Journal Supplement Series*, 211, 12
- Guilbert, P. W., Fabian, A. C., & Rees, M. J. 1983, *MNRAS*, 205, 593
- Hamburg, R., Veres, P., Meegan, C., et al. 2019, GRB Coordinates Network, Circular Service, No. 23707, #1 (2019), 23707
- He, H.-N., Wu, X.-F., Toma, K., Wang, X.-Y., & Mészáros, P. 2011, *ApJ*, 733, 22
- Hoischen, C., Balzer, A., Bissaldi, E., et al. 2017, *International Cosmic Ray Conference*, 35, 636
- Hurley, K., Dingus, B. L., Mukherjee, R., et al. 1994, *Nature*, 372, 652
- Kalberla, P. M. W., Burton, W. B., Hartmann, D., et al. 2005, *A&A*, 440, 775
- Kaneko, Y., Preece, R. D., Briggs, M. S., et al. 2006, *The Astrophysical Journal Supplement Series*, 166, 298
- Kocevski, D., Omodei, N., Axelsson, M., et al. 2019, GRB Coordinates Network, Circular Service, No. 23709, #1 (2019), 23709
- Kumar, P. & Barniol Duran, R. 2009, *MNRAS*, 400, L75
- Kumar, P. & Barniol Duran, R. 2010, *MNRAS*, 409, 226
- Kumar, P., Hernández, R. A., Bošnjak, Ž., & Barniol Duran, R. 2012, *MNRAS*, 427, L40
- Lyutikov, M. 2010, *MNRAS*, 405, 1809
- Meegan, C., Lichti, G., Bhat, P. N., et al. 2009, *ApJ*, 702, 791
- Minaev, P. & Pozanenko, A. 2019, GRB Coordinates Network, Circular Service, No. 23714, #1 (2019), 23714
- Mirzoyan, R., Noda, K., Moretti, E., et al. 2019, GRB Coordinates Network, Circular Service, No. 23701, #1 (2019), 23701
- Molinari, E., Vergani, S. D., Malesani, D., et al. 2007, *A&A*, 469, L13
- Nava, L., Desiante, R., Longo, F., et al. 2017, *MNRAS*, 465, 811
- Nava, L., Ghirlanda, G., Ghisellini, G., & Celotti, A. 2011, *A&A*, 530, A21
- Nava, L., Sironi, L., Ghisellini, G., Celotti, A., & Ghirlanda, G. 2013, *MNRAS*, 433, 2107
- Nava, L., Vianello, G., Omodei, N., et al. 2014, *MNRAS*, 443, 3578
- Oganesyan, G., Nava, L., Ghirlanda, G., & Celotti, A. 2017, *ApJ*, 846, 137
- Oganesyan, G., Nava, L., Ghirlanda, G., & Celotti, A. 2018, *A&A*, 616, A138
- Omodei, N. 2009, in *American Institute of Physics Conference Series*, Vol. 1112, American Institute of Physics Conference Series, ed. D. Bastieri & R. Rando, 8–15
- Panaitescu, A. 2017, *ApJ*, 837, 13
- Rao, A., Basak, R., Bhattacharya, J., et al. 2013, *Research in Astronomy and Astrophysics*, 14
- Ravasio, M. E., Oganesyan, G., Ghirlanda, G., et al. 2018, *A&A*, 613, A16
- Romano, P., Campana, S., Chincarini, G., et al. 2006, *A&A*, 456, 917
- Sari, R. & Piran, T. 1999, *ApJ*, 520, 641
- Selsing, J., Fynbo, J. P. U., Heintz, K. E., et al. 2019, GRB Coordinates Network, Circular Service, No. 23695, #1 (2019), 23695
- Sommer, M., Bertsch, D. L., Dingus, B. L., et al. 1994, *ApJ*, 422, L63
- Toma, K., Wu, X.-F., & Mészáros, P. 2011, *MNRAS*, 415, 1663
- Ursi, A., Tavani, M., Marisaldi, M., & et al. 2019, GRB Coordinates Network, Circular Service, No. 23712, #1 (2019), 23712
- Uzdensky, D. A., Cerutti, B., & Begelman, M. C. 2011, *ApJ*, 737, L40
- Wang, Y., Li, L., Moradi, R., & Ruffini, R. 2019, *arXiv e-prints*, arXiv:1901.07505
- Wilms, J., Allen, A., & McCray, R. 2000, *ApJ*, 542, 914
- Xiao, S., Li, C. K., Li, X. B., et al. 2019, GRB Coordinates Network, Circular Service, No. 23716, #1 (2019), 23716
- Yassine, M., Piron, F., Mochkovitch, R., & Daigne, F. 2017, *A&A*, 606, A93
- Yonetoku, D., Murakami, T., Nakamura, T., et al. 2004, *ApJ*, 609, 935
- Zhang, B.-B., Zhang, B., Liang, E.-W., et al. 2011, *ApJ*, 730, 141